Nanoscale Horizons

ROYAL SOCIETY OF CHEMISTRY

COMMUNICATION

View Article Online
View Journal | View Issue

Cite this: *Nanoscale Horiz.*, 2025, **10**, 905

Received 7th January 2025,
Accepted 27th February 2025

DOI: 10.1039/d5nh00013k

rsc.li/nanoscale-horizons

Enhanced photothermal methane dry reforming through electronic interactions between nickel and yttrium†

Xueying Zhang,[abc] Zeshu Zhang,*[abc] Qishun Wang,[cd] Jianheng Xu,[abc] Xinyu Han,[abc] Jiakun Wang,[abc] Jia Liu,[abc] Cheng Rao,[abc] Xiangguang Yang,[abc] Yibo Zhang*[abc] and Lu Wang *[e]

Dry reforming of methane (DRM) is a promising technology for converting greenhouse gases (CH_4 and CO_2) into syngas. However, the traditional thermal catalytic process requires high temperature, resulting in low selectivity, and coke-induced instability. In this study, a Y-doped nickel-based photothermal catalyst, NiY/fibrous nano-silica (KCC-1), was obtained for the DRM reaction, exhibiting excellent photothermal catalytic DRM activity with a CO yield rate of above 90.01 mmol g^{-1} h^{-1} at 450 °C. The spatial confinement effect of KCC-1 enhanced the catalyst stability, maintaining fresh activity for up to 40 hours. Various characterization techniques reveal that strong d-electron transfer from Y to Ni is beneficial for preserving metallic Ni, which in turn promotes the adsorption and activation of CH_4. *In situ* DRIFTS and DFT theoretical studies further elucidate the mechanism that the Y-doped strategy not only facilitates the adsorption and activation of CO_2 (due to the strong basicity of Y_2O_3) but also enhances the photothermal effect by facilitating the formation of metallic Ni^0, resulting in a greater generation of p-CO_3^{2-} intermediates to achieve excellent photothermal catalytic performance. The findings of this study are expected to provide a rare earth metal doping strategy for designing highly efficient photothermal catalysts for the synthesis of solar fuel.

1. Introduction

The accumulation of carbon dioxide (CO_2) and methane (CH_4) in the atmosphere has intensified the greenhouse effect, attracting widespread attention from academia and industry.[1–4] Countries are actively researching methane–carbon dioxide reforming (DRM, $CO_2 + CH_4 \rightarrow CO + H_2$) technology, which can effectively resource these two greenhouse gases (methane and carbon dioxide), mitigate the greenhouse effect, and simultaneously generate industrial syngas (CO and H_2).[5–7] However, due to the endothermic nature of this reaction (ΔH_{298K} = 247 kJ mol^{-1}), conventional thermal catalytic reforming necessitates exceedingly high temperatures, exceeding 650 °C.[8–10] The active metal particles (*e.g.*, Pt, Ru, Pd, Ni, and Co) supported on catalysts, due to their nanoscale properties, exhibit lower sintering temperatures (<600 °C) and are then susceptible to sintering.[11–14] Furthermore, methane thermodynamically tends to crack into coke above 600 °C, obstructing active sites and leading to catalyst deactivation.[15]

Nickel-based (Ni-based) catalysts are extensively utilized and researched in DRM due to their superior C–H bond cleavage capabilities and cost-effective synthesis.[16] However, due to the relatively low Tammann temperature of nickel (581 °C), Ni

[a] *School of Rare Earths, University of Science and Technology of China, Hefei 230026, China. E-mail: zszhang@gia.cas.cn, yibozhang@gia.cas.cn*
[b] *Ganjiang Innovation Academy, Chinese Academy of Sciences, No. 1, Science Academy Road, Ganzhou 341000, China*
[c] *Key Laboratory of Rare Earths, Chinese Academy of Sciences, Ganzhou 341000, China*
[d] *Changchun Institute of Applied Chemistry, Chinese Academy of Sciences, Changchun, 130022, China*
[e] *School of Science and Engineering, The Chinese University of Hong Kong, Shenzhen, 518172, Guangdong, China. E-mail: lwang@cuhk.edu.cn*

† Electronic supplementary information (ESI) available. See DOI: https://doi.org/10.1039/d5nh00013k

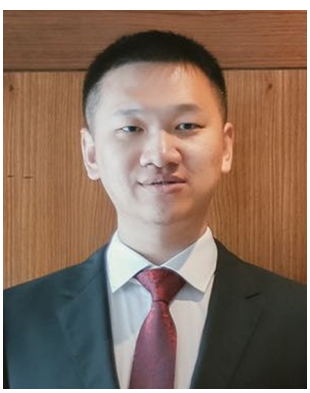

Lu Wang

In celebration of the 10th Anniversary of Nanoscale Horizons, we are honored to present our inaugural contribution to this distinguished journal. Our work underscores the remarkable potential of nanomaterial architectures in advancing photothermal catalytic methane dry-reforming systems. By showcasing a rationally designed catalyst, we demonstrate transformative strategies for solar energy conversion and the utilization of greenhouse gases to produce syngas. Congratulations to Nanoscale Horizons on this milestone; we would like to keep contributing to the journal and extend our best wishes for continued success in the years to come.

nanoparticles are highly susceptible to sintering at the operational temperatures employed in dry reforming of methane (DRM).[17,18] Additionally, the formation of larger Ni nanoparticles through sintering or agglomeration brings active sites into closer proximity, which favors successive C–H bond cleavage and subsequent C–C coupling.[19] This leads to severe coke formation and thus limits the catalyst's lifetime. For example, Mustu *et al.* synthesized Ni-containing mesoporous zirconia catalysts (Ni@ZrO_2–C) for the DRM reaction at 600 °C for only 4 hours, resulting in significant coking that accounted for 14% of the catalyst's weight.[20] Therefore, achieving high catalytic activity under mild conditions while minimizing sintering and carbon deposition remains a formidable challenge for Ni-based catalysts. As a renewable and clean energy source, solar energy optimizes the methane reforming reaction under mild conditions, surpassing thermodynamic limitations and reducing dependence on fossil fuels.[21–23] However, traditional photocatalysis has low efficiency due to the recombination rate of photogenerated electron–hole pairs being higher than the surface catalytic reaction rate.[24,25] Emerging photothermal catalysis combines the benefits of photocatalysis and thermal catalysis, substantially lowering reaction barriers and achieving high conversion rates, thereby enhancing the catalytic efficiency.[26,27] Traditional wisdom for improving the photothermal catalytic performance mainly relies on defects, doping, morphology, and structure engineering. Among these strategies, elemental doping is a cost-effective and straightforward method to enhance the catalytic performance by tuning the band structure and electronic properties of the material.[28–30] For example, Zhang *et al.* significantly enhanced the catalytic performance of DRM over the NiCo alloy nanoparticle catalyst by the photothermal effect, achieving more than a twofold increase in efficiency. Nonetheless, the incorporation of Co intensified the redox properties excessively, leading to undesirable side reactions.[31] When selecting doping elements, it is crucial to consider the adsorption capacity of the reactants and the redox capacity of the catalyst, to promote the reaction between CH_4 and CO_2 while inhibiting other side reactions.

In this study, KCC-1 zeolite with an ordered pore structure was employed to spatially confine Ni nanoparticles, and Y element (with a strong Lewis basicity[32]) doping was performed to enhance the photothermal CH_4–CO_2 reforming reaction performance. The strong d-electron transfer between Ni and Y optimized the band structure and augmented the photothermal effect, achieving a CO generation rate of 90.01 mmol g^{-1} h^{-1} at 450 °C. Additionally, the electronic interaction and the confinement effect of KCC-1 collectively enhanced the stability of the Ni-based catalyst, maintaining its initial activity for 40 hours. Therefore, this study demonstrates that doping modification can optimize the band structure of materials through electronic interactions, significantly improving photothermal catalytic performance, and offering a new idea for efficient and stable photothermal catalysis.

2. Experimental

2.1. Catalyst preparation

2.1.1. Preparation of NiY/KCC-1. The synthetic method of KCC-1 has been reported in the previous references (ref. 33 and 34). As shown in Scheme 1, $Ni(NO_3)_2{\cdot}6H_2O$ (0.0495 g) and $Y(NO_3)_3{\cdot}6H_2O$ (0.0456 g) were dissolved in ethylene glycol (600 μL), and KCC-1 (200 mg) was added. The mixture was stirred at room temperature for 2 h and dried at 80 °C. Finally, the dried product was calcined at 500 °C for 5 h to obtain the sample (denoted as NiY/KCC-1, 5 wt% Ni).

2.1.2. Preparation of other catalysts. For comparative purposes, two reference catalysts were synthesized: KCC-1-supported single Ni (denoted as Ni/KCC-1, 5 wt% Ni) and SiO_2-supported NiY (denoted as NiY/SiO_2, 5 wt% Ni). The preparation process of these catalysts was identical to the procedure described above.

2.2. DRM performance evaluation

A fixed-bed microreactor was utilized to evaluate the photothermal catalytic performance of methane dry reforming, and Fig. S1 (ESI†) illustrates a schematic representation of the equipment and procedures involved.[35] The light source employed is a xenon lamp with variable power settings (Beijing Perfectlight, PLS-SXE300+). The light intensity was calibrated

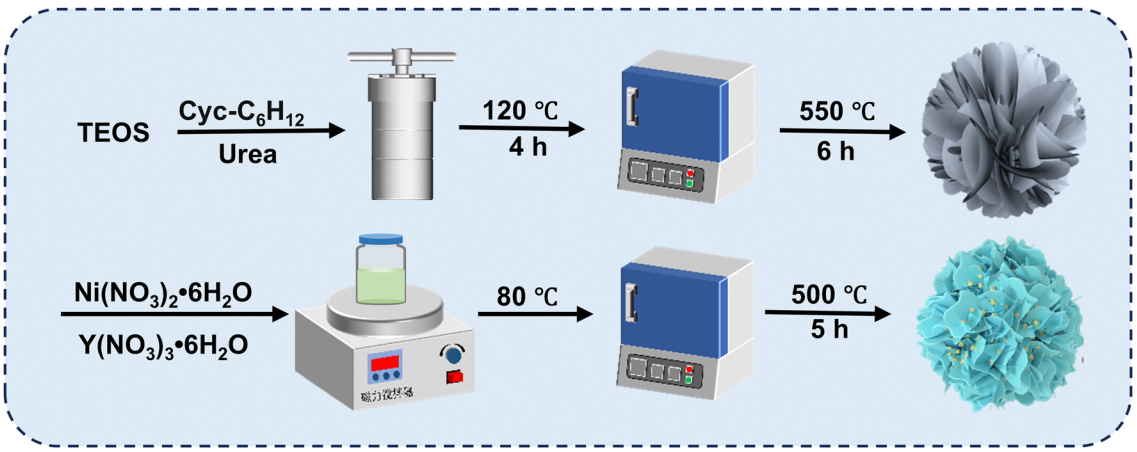

Scheme 1 Synthesis flowchart of the catalyst.

with an optical power meter (Perfectlight, PL-MW2000). The light-receiving area of the sample section was approximately 1 cm^2. The thermocouple was inserted into the quartz tube and positioned above the catalyst. Weight hourly space velocity (WHSV) is 12 000 mL h^{-1} g^{-1}. A mixture of 250 mg of quartz sand (40–60 mesh) and 50 mg of catalyst is prepared and placed in a quartz tube. By reducing pure hydrogen at 700 °C for 1 h, the hydrogen flow rate is 10 mL min^{-1}. The gas flow rate was maintained at 10 mL min^{-1}, and the quartz tube was connected to a ternary gas mixing system with a composition of CH_4 : CO_2 : Ar = 4 : 4 : 2. After the reaction, the syngas passed through 5A and HQ packed columns. Each component in the syngas was separated based on their distinct retention times, and the CO concentration in the reaction exhaust gas was monitored using a thermal conductivity detector (TCD) gas chromatograph.[36] The formation rate of CO is calculated using eqn (1):

$$r = \frac{60V[\mathrm{CO}]_{\mathrm{out}}}{100 \times 22.4m} \quad (1)$$

where r represents the rate of CO formation, mmol g^{-1} h^{-1}. V represents the gas flow rate in the system, mL h^{-1}. $[CO]_{out}$ represents the proportion of CO exports, %. 22.4 represents the molar volume of an ideal gas at standard temperature and pressure conditions, L mol^{-1}. m represents the mass of the catalyst, g.

Subsequently, the natural logarithm (ln) is applied to the CO formation rate r. The relationship between the natural logarithm of the catalyst's CO formation rate, ln(r), and the test temperature T is derived from eqn (2):

$$\ln r = -\frac{E_a}{1000RT} + C \quad (2)$$

where r represents the formation rate of CO, mmol g^{-1} h^{-1}. E_a represents the activation energy of the catalyst, J mol^{-1}. R is the ideal gas constant, 8.314 J mol^{-1} K^{-1}; T represents the test temperature, K. C represents the pre-reference factor.

2.3. Catalyst characterization

The X-ray diffraction (XRD) patterns of these catalysts were acquired using a Bruker D8 Advance system, employing Ni-filtered Cu Kα radiation (λ = 0.15418 nm). Transmission electron microscopy (TEM) images were taken with a Talos F200x using an FEI CCD camera with an accelerating voltage of 200 kV. The N_2 isotherm adsorption and desorption tests were performed using an ASAP2460 (Micromeritics). The pore size distribution of the catalyst was determined using the Barrett–Joyner–Halenda (BJH) method.

X-ray photoelectron spectroscopy (XPS) was performed using a Thermo Scientific K-Alpha XPS system with Al Kα as the excitation source. The binding energy was calibrated by C 1s = 284.80 eV. H_2-temperature programmed reduction (H_2-TPR) was performed using a BSD-Chem C200 chemisorption analyzer from BSD Instrument, Beijing. About 200 mg of catalyst was filled in the quartz tube. Before the test, the catalyst was pretreated in high-purity argon at 300 °C for 1 h at a flow rate of 30 mL min^{-1} and then cooled to room temperature. Subsequently, a 10% H_2–Ar gas mixture was introduced into the apparatus at a flow rate of 30 mL min^{-1}. Simultaneously, the heater was ramped up to 800 °C at a heating rate of 10 °C min^{-1}, during which the TCD detector signal was continuously recorded. CO_2-temperature programmed desorption (CO_2-TPD) was also carried out using a BSD Chem-C200 analyzer. After pretreatment with Ar at 300 °C for 1 hour, the catalyst was exposed to a 5% CO_2–Ar mixture at a flow rate of 30 mL min^{-1} at 50 °C for 1 hour. Pure Ar gas was then pumped into the system to purge physically adsorbed CO_2 and held for 30 minutes. Subsequently, the TCD detector was activated, and the temperature was increased to 800 °C while maintaining the Ar flow to complete the desorption data recording. For CH_4-temperature programmed desorption (CH_4-TPD), the 5% CO_2–Ar mixture was replaced with a 4% CH_4–N_2 mixture, with all other settings remaining unchanged.

In situ DRIFTS was performed in the wave number range of 4000 to 650 cm^{-1} by accumulating 32 scans on a Nicolet iS50 FT-IR spectrometer equipped with Harrick DRIFTS batteries and a liquid nitrogen-cooled high-sensitivity MCT detector. 5 mg of catalyst with KBr as a substrate was injected into the sample chamber and the background was collected under a Ar atmosphere. *In situ* infrared tests were performed at different temperatures, the feedstock gas was switched to 5% CO_2–Ar and 4% CH_4–N_2, respectively, and the temperature was increased to 100 °C, 200 °C, 300 °C, and 400 °C for several minutes to record the spectrum. In the pre-adsorption experiment, after the background was collected in an Ar atmosphere, the feed gas was switched to 5% CO_2–Ar (or 4% CH_4–N_2) for adsorption to equilibrium, and then the feed gas was switched to 4% CH_4–N_2 (5% CO_2–Ar) for several minutes to record the spectrum. In the simultaneous adsorption experiment of CO_2 and CH_4, after the background was collected in an Ar atmosphere, the feedstock gas was switched to a mixture of 5% CO_2–Ar and 4% CH_4–N_2 for several minutes to record the spectrum.

3. Results and discussion

3.1. Catalytic performance of samples

The photothermal catalytic DRM performance of 5%$Ni_{10}Y_5$/KCC-1, 5%$Ni_{10}Y_7$/KCC-1, 5%$Ni_{10}Y_9$/KCC-1 and 5%$Ni_{10}Y_{11}$/KCC-1 is shown in Fig. S2 (ESI†). As the concentration of Y increases, the catalytic performance displays a volcano plot, with 5%$Ni_{10}Y_7$/KCC-1 (referred to as NiY/KCC-1) demonstrating the best catalytic activity, surpassing the thermodynamic equilibrium conversion. In Fig. 1a, with an increase in temperature (250 °C to 450 °C), the photothermal catalytic performance over NiY/KCC-1 increases, and the CO formation rate over NiY/KCC-1-light (90.01 mmol g^{-1} h^{-1}) at 450 °C is about 100% enhancement compared with that of Ni/KCC-1-light. Additionally, under light-only conditions, NiY/KCC-1 exhibited a CO formation rate of 43.37 mmol g^{-1} h^{-1} (Fig. 1b), twice higher than that of Ni/KCC-1 (16.09 mmol g^{-1} h^{-1}). In Fig. 1c, as the light intensity increases, the heating rate and apparent temperature of NiY/KCC-1 were higher than that of Ni/KCC-1, demonstrating that Y-doping could boost the photothermal effect. In addition, the catalytic performance was boosted when exposed to a higher light intensity, and the rate of CO was

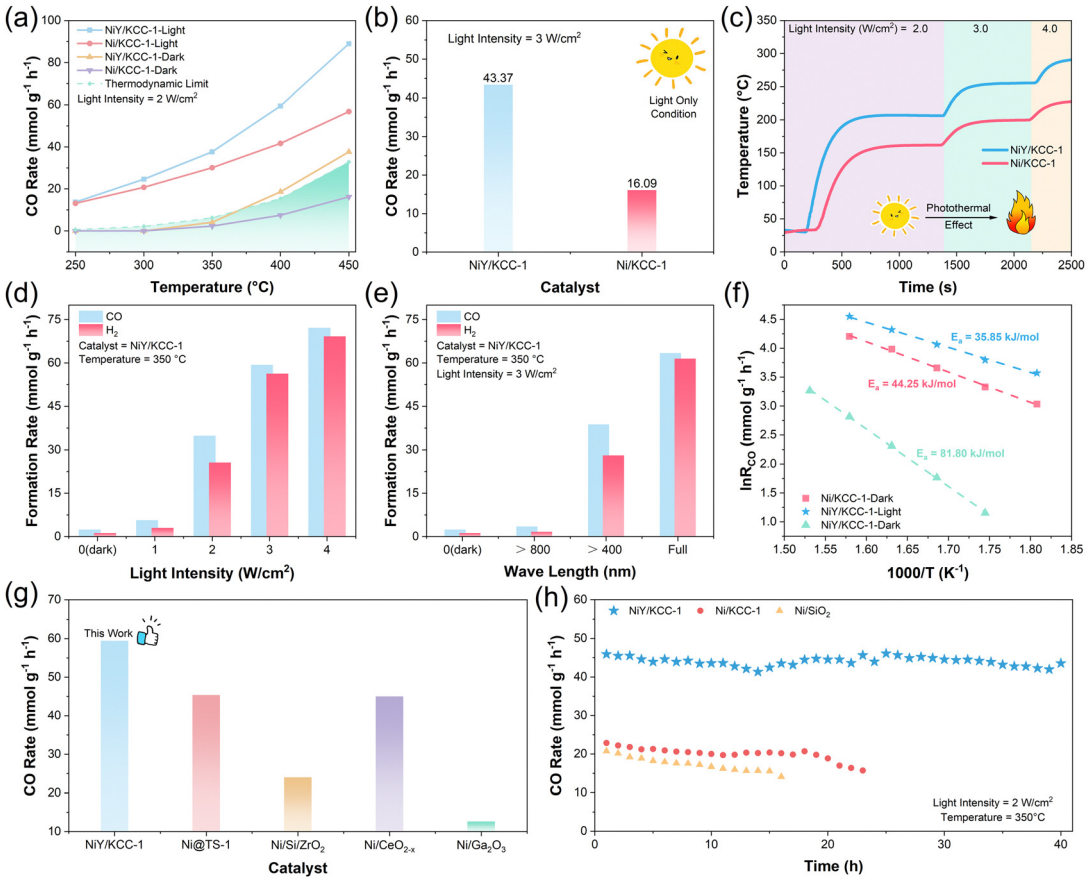

Fig. 1 CO formation rate of the NiY series of catalysts at (a) different temperatures; (b) CO formation rate of NiY/KCC-1 under light without an external heating source; (c) the temperature of Ni/KCC-1 and NiY/KCC-1 at different light intensities; CO and H_2 formation rates of Ni/KCC-1 and NiY/KCC-1 at (d) different light intensities at 350 °C and (e) different wavelengths at 350 °C; (f) Arrhenius plots of Ni/KCC-1 and NiY/KCC-1 under dark and light; (g) CO formation rate of different catalysts at 400 °C; (h) evolution of the CO formation rate with time for the NiY series of catalysts.

recorded to be up to 72.13 mmol g^{-1} h^{-1} under an illumination of approximately 40 suns (Fig. 1d).

The wavelength of light significantly affects the catalyst performance, as illustrated in Fig. 1e. The catalyst exhibits poor absorption for wavelengths above 800 nm, resulting in a low DRM reaction rate under such illumination. Conversely, when the wavelength is adjusted to below 400 nm, both CO and H_2 generation rates increase markedly, indicating that the catalyst exhibits significant absorption capacity in the 400 to 800 nm range. It is noted that despite the change in light intensity and wavenumber, the ratio of CO/H_2 approached 1 : 1 and the light-to-fuel efficiency is stable at about 3.5% at a light intensity of above 2 W cm^{-2} (Fig. S5, ESI†). This finding suggests a low incidence of side reactions on the catalyst surface, implying that the catalyst exhibits a moderate redox capacity.[37]

The activation energy of the catalyst under both light and dark conditions was also determined, with the results presented in Fig. 1f. The activation energy of NiY/KCC-1 for a catalytic DRM reaction remains comparable in the presence (35.8 kJ mol^{-1}) and absence (81.8 kJ mol^{-1}) of light, proving that light exposure plays a vital role in reducing the activation energy required for the DRM reaction. It was worth noting that the activation energy of Ni/KCC-1 (44.2 kJ mol^{-1}) under light is similar to that of NiY/KCC-1, suggesting identical active sites for the DRM reaction regardless of Y-doping. Furthermore, the photothermal catalytic activity over NiY/KCC-1 has a huge advantage compared to other reported references, as shown in Fig. 1g.[38–41] In Fig. 1h, the CO formation rate can retain the fresh catalytic activity during the 40-hour stability tests, while deactivation was obvious for Ni/KCC-1 and NiY/SiO_2 in the first 20 hours, proving that Y-doping effectively regulates the redox properties of the Ni-based catalyst, enhances the DRM reaction rate and inhibits carbon deposition. Additionally, thermogravimetric analysis (TGA) of the post-reaction catalysts (Fig. S6, ESI†) revealed a lower carbon accumulation rate for used NiY/KCC-1 (0.0008 h^{-1}) compared to NiY/SiO_2 (0.0216 h^{-1}), indicating that the pore-space confinement effect of KCC-1 significantly improves the catalyst stability.

3.2. Physical and chemical properties of catalysts

In Fig. 2a, the XRD patterns of $5\%Ni_{10}Y_7$/KCC-1 showed diffraction peaks of elementary substance Ni^0 at 44.6°, 51.9° and 76.5° (PDF#04-004-8868). In contrast, the XRD patterns of 5%Ni/KCC-1 showed diffraction peaks of NiO at 37.2°, 43.2° and 62.8° (PDF#97-006-1544), indicating that Y doping is beneficial for maintaining the metallic state of Ni. Generally speaking, Ni^0 is the active site over the Ni-based catalysts for DRM,[42]

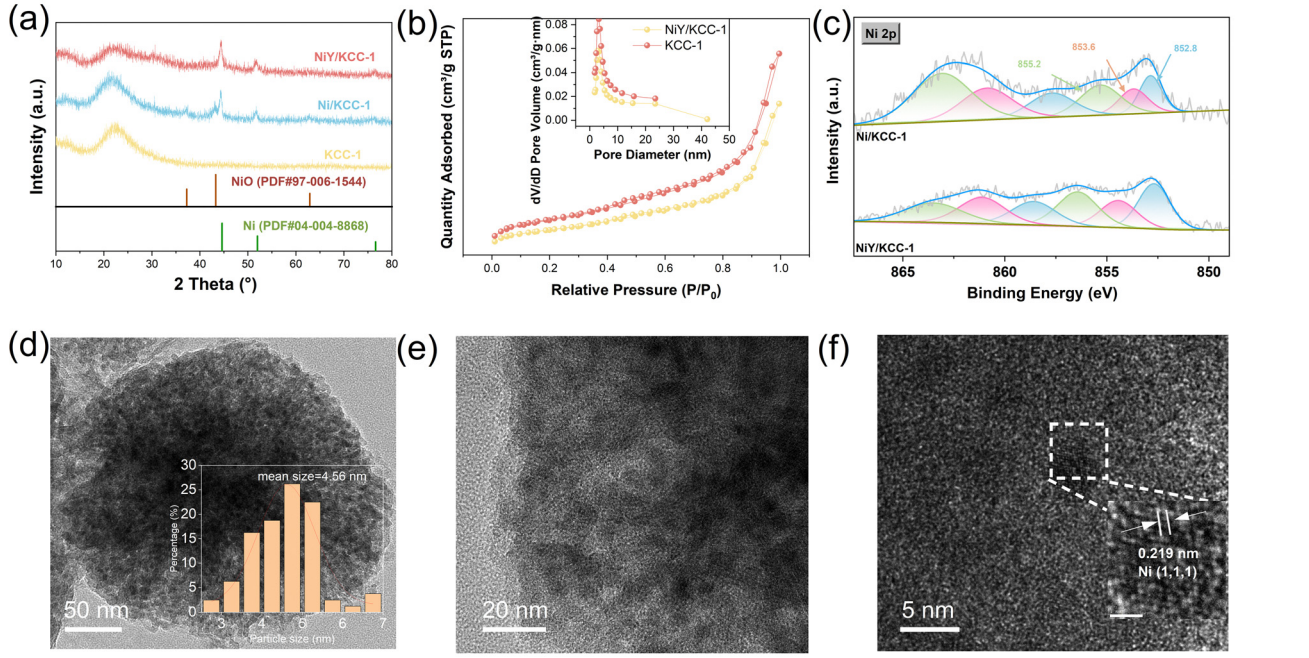

Fig. 2 (a) XRD patterns of Ni/KCC-1 and NiY/KCC-1 catalysts and KCC-1; (b) N_2 adsorption–desorption curves and pore width distributions of Ni/KCC-1 and NiY/KCC-1 catalysts; (c) XPS of Ni2p; (d)–(f) HR-TEM images and locally enlarged images of NiY/KCC-1.

and therefore, the huge activity advantage of NiY/KCC-1 over Ni/KCC-1 was exhibited. Additionally, the images of SEM (Fig. S7, ESI†) also revealed that the incorporation of Ni and Y did not change the morphology and structure of KCC-1. In Fig. 2b the N_2 isotherm adsorption–desorption curves of KCC-1 and NiY/KCC-1 showed that both exhibit abundant mesoporous structures, with a pore size of about 2.90 nm and 2.32 nm, respectively. This implies that Ni and Y are dispersed within the pore of KCC-1, reducing the pore size of pure KCC-1. X-ray photoelectron spectroscopy (XPS) analyses of Ni/KCC-1 and NiY/KCC-1 are shown in Fig. 2c. The binding energy at 852.8 eV, 855.2 eV, and 857.6 eV were attributed to elemental Ni^0, NiO, and NiOH, respectively. The peak position of Ni in NiY/KCC-1 shifted to a lower binding energy compared to Ni/KCC-1. Meanwhile, the NiO/Ni ratio in NiY/KCC-1 decreased due to the electron transfer from Y to Ni. This is consistent with the XRD analysis results that more Ni^0 is present in NiY/KCC-1, thus confirming the electron transfer between Y and Ni. The NiY particles in NiY/KCC-1 were evenly dispersed throughout the pores, as observed in the high-resolution transmission electron microscopy (HR-TEM) images in Fig. 2d. The average Ni particle size of NiY/KCC-1 was 4.56 nm. The energy-dispersive X-ray spectrometry (EDS) elemental mapping images (Fig. S8, ESI†) showcased the uniform distribution of Ni, O, Si, and Y.

According to the UV-Vis-NIR spectra, NiY/KCC-1 exhibits superior light absorption properties compared to Ni/KCC-1(Fig. S9, ESI†), enabling it to convert more light energy into heat, thereby elevating the local temperature of the catalyst and promoting the DRM reaction.[43]

The redox capacity of the catalysts and the adsorption capacity of the reactants were assessed. In Fig. 3a, the H_2-TPR profiles of NiY/KCC-1 and Ni/KCC-1 exhibited two reduction regions, the α region and the β region. The α region corresponds to the reduction of highly dispersed NiO on the KCC-1 surface,[44] while the β region corresponds to the reduction of NiO species interacting with SiO_2 and lattice oxygen on the SiO_2 surface. The α region showed that the reduction peak of NiY/KCC-1 is smaller than that of Ni/KCC-1, and the reduction peak shifts to a higher temperature, indicating fewer forms of NiO in the surface NiY/KCC-1 catalyst. For the β region, due to the interaction of NiO with Y_2O_3 and SiO_2, NiY/KCC-1 exhibited a higher reduction temperature. These H_2-TPR results are consistent with XRD and XPS results, indicating electron transfer from Y to Ni in NiY/KCC-1 and that the catalyst is predominantly metallic Ni. In the CO_2-TPD curves, the physical adsorption peak (100 °C) and chemical adsorption peak (250 °C to 650 °C) of CO_2 on NiY/KCC-1 are stronger than those on Ni/KCC-1 (Fig. 3b). Since Y is close to alkaline earth metals, Y doping in NiY/KCC-1 increases the basicity of the catalyst, enhancing CO_2 adsorption. In the CH_4-TPD curves (Fig. 3c), Y doping enhances the methane adsorption capacity of the NiY/KCC-1 sample across both the low-temperature physical adsorption and high-temperature chemical adsorption regions, as electrons transfer from Y to Ni, thereby increasing the amount of metallic Ni. The above results indicate that the strong adsorption capacity of CO_2 and CH_4 on NiY/KCC-1 ensures that NiY/KCC-1 shows excellent DRM catalytic performance.

In situ DRIFTS is also employed to detect the adsorption of CO_2 and CH_4 of the NiY/KCC-1 catalyst. In the *in situ* DRIFT spectra of the adsorption of CO_2 shown in Fig. 3d and Fig. S10a (ESI†), the adsorption peaks of CO are located approximately at 1920 cm^{-1} and 1819 cm^{-1}, the adsorption peak of carbonates is

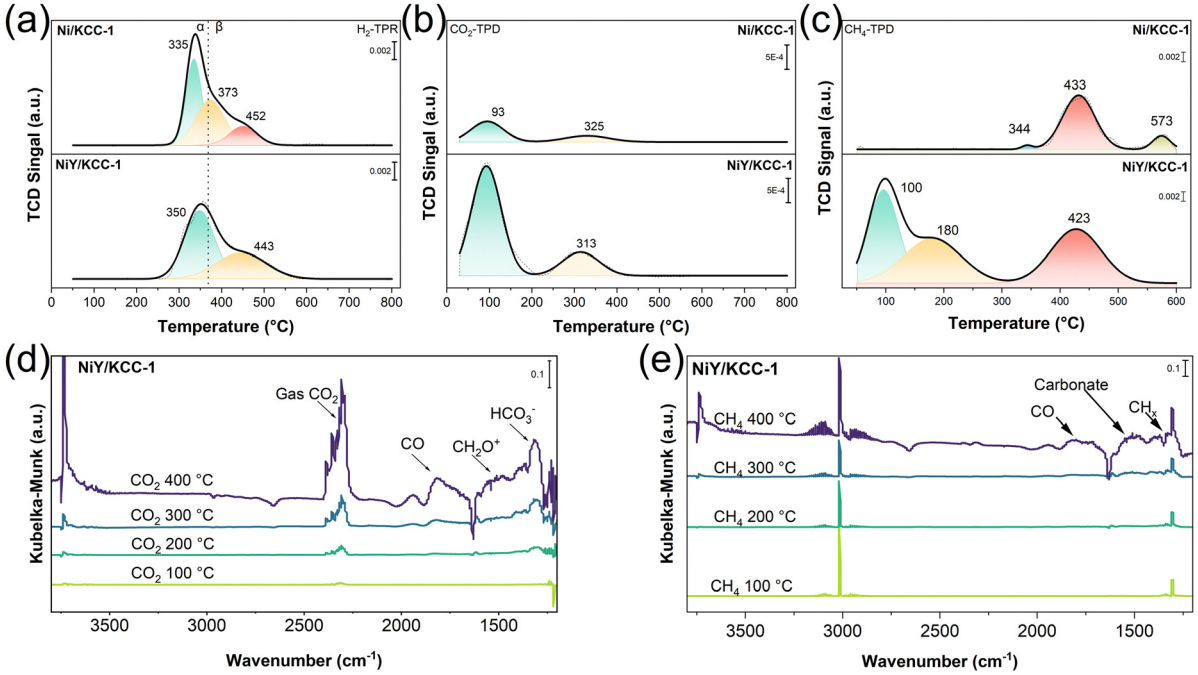

Fig. 3 (a) H_2-TPR, (b) CO_2-TPD, and (c) CH_4-TPD of Ni/KCC-1 and NiY/KCC-1; *in situ* DRIFT spectra of the adsorption of (d) CO_2 and (e) CH_4 at various temperatures of NiY/KCC-1 under light.

at around 1508 cm^{-1}, and the adsorption peak of HCO_3^- is around 1306 cm^{-1}.[11] It can be observed that these intermediates appear on the NiY/KCC-1 catalyst at 200 °C under light irradiation, whereas they only appear on the Ni/KCC-1 catalyst above 400 °C, indicating that NiY/KCC-1 has superior CO_2 activation capability. Under light, the catalyst was also exposed to a 4% CH_4–N_2 gas stream, and adsorption experiments were conducted at 100 °C, 200 °C, 300 °C, and 400 °C, as shown in Fig. 3e and Fig. S10b (ESI†). Peaks at 1803 cm^{-1} and 1938 cm^{-1} correspond to CO adsorption species, 1517 cm^{-1} corresponds to carbonate adsorption species, and 1326 cm^{-1} corresponds to CH_x adsorption. Notably,[41,45] NiY/KCC-1 can activate methane at 300 °C to produce these intermediates, while intermediates show on the Ni/KCC-1 surface up to 400 °C, further demonstrating that NiY/KCC-1 has superior CH_4 activation ability. Meanwhile, it was observed that the temperature required to activate CH_4 on NiY/KCC-1 is higher than that for CO_2, indicating that CH_4 activation is the key step in the DRM reaction. Given that metallic Ni has a higher CH_4 adsorption activation capability than NiO,[46] the NiY/KCC-1 catalyst with more metallic Ni exhibits higher catalytic performance (Fig. 3d and e). Therefore, *in situ* DRIFT spectra of the adsorption of CO_2 and CH_4 are consistent with the results from the CO_2-TPD and CH_4-TPD experiments, explaining the photothermal activity advantage of NiY/KCC-1 over Ni/KCC-1.

3.3. *In situ* DRIFTS study

To further investigate the potential mechanism of the DRM reaction on catalyst surfaces, *in situ* DRIFT spectra were recorded for the NiY/KCC-1 and Ni/KCC-1 catalysts. In Fig. 4(a–c), when exposed to a CO_2/Ar atmosphere under light conditions, the intensity of the CO_2 absorption peak on the NiY/KCC-1 surface changed slowly after switching to the CH_4 atmosphere, compared to observations in the dark. This indicates that NiY/KCC-1 is more favorable to CO_2 adsorption under light conditions. Since HCOO* (1374 cm^{-1}, 1398 cm^{-1}) species were detected on NiY/KCC-1 and Ni/KCC-1 under dark conditions, where HCOO* reacts with H* species to produce HCOOH, further dissociating into H_2O.[45] This represents a side reaction in the DRM process, resulting in lower catalytic efficiency under dark, as light inhibits these side reactions. In contrast, the sample was initially exposed to CH_4 for 20 min before being switched to a CO_2 atmosphere, as shown in Fig. 4(d–f). On the NiY/KCC-1 catalyst, bidentate carbonates (b-CO_3^{2-}, 1617 cm^{-1})[47–49] and multidentate carbonates (p-CO_3^{2-}, 1500 cm^{-1})[47–49] were observed under light and dark conditions, while the Ni/KCC-1 surface showed minimal carbonate intermediate formation. This indicates that the addition of Y is conducive to the adsorption and activation of CO_2, due to the alkaline properties. Furthermore, comparing the experiments where Ni/KCC-1 first adsorbed CO_2 (Fig. 4c) and CH_4 (Fig. 4f) reveals that there is competitive adsorption of CO_2 and CH_4 in this reaction, with Y providing additional adsorption sites for CO_2.

When CH_4 and CO_2 are introduced simultaneously, the spectrum of NiY/KCC-1 resembles that in Fig. 4a and d, featuring intermediate species like CO_3^{2-}, CH_x, CO, and OH.[41,45] Notably, under light conditions, the b-CO_3^{2-} peak at 1617 cm^{-1} decay fast (Fig. 5a), while its decomposition is more difficult in the dark (Fig. 5b). Since CO production is linked to the decomposition of carbonates, light facilitates this process, resulting in increased CO generation, as evidenced by the increased intensity of the CO absorption peak. In the absence of light (Fig. 5b), the NiY/KCC-1 catalyst exposed to CH_4 and CO_2 exhibits a high-intensity OH

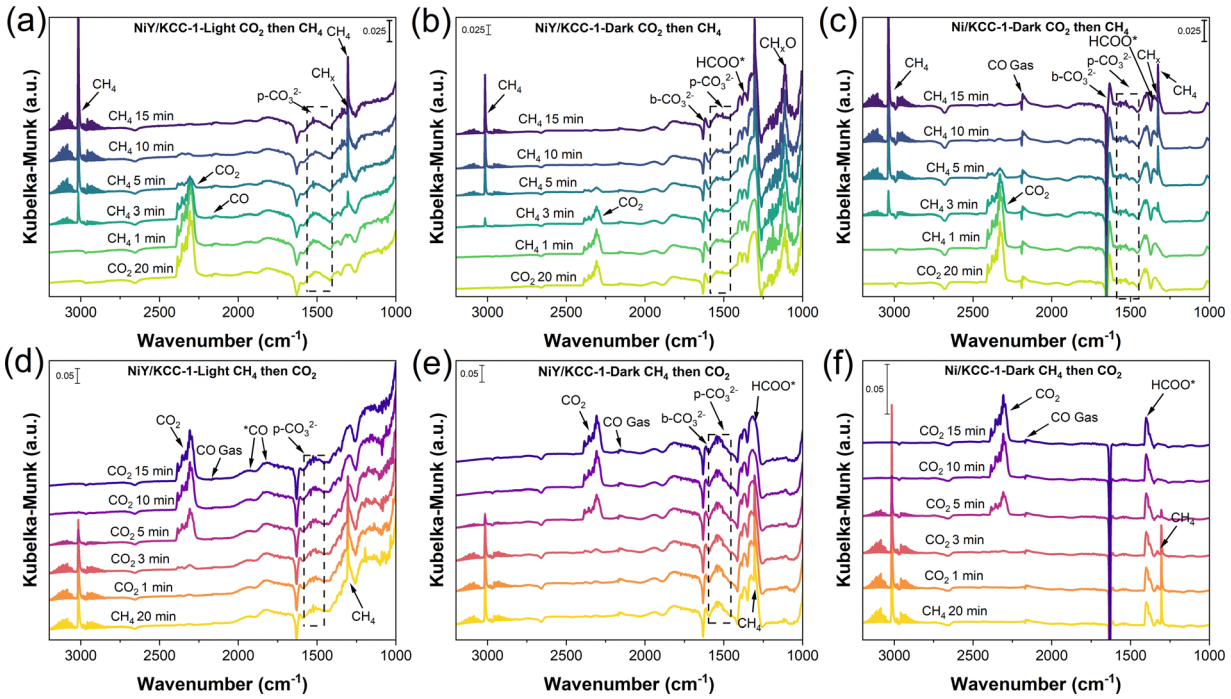

Fig. 4 (a) and (b) *In situ* DRIFT spectra of species adsorbed on NiY/KCC-1 by first passing CO_2 and then CH_4 under (a) light and (b) dark conditions; (c) *in situ* DRIFT spectra of species adsorbed by CO_2 and then CH_4 on Ni/KCC-1 under dark conditions; (d) and (e) *in situ* DRIFT spectra of species adsorbed by CH_4 and then CO_2 on NiY/KCC-1 under (d) light and (e) dark conditions; and (f) *in situ* DRIFT spectra of adsorbed species on Ni/KCC-1 through CH_4 and then CO_2 under dark conditions.

group infrared absorption peak at around 3700 cm^{-1},[50] indicating substantial water formation on the surface. This aligns with the significant decomposition of HCOO* into H_2O, as shown in Fig. 4b and e. Thus, light irradiation inhibits the hydrogenation reaction between H species and oxygen-containing substances, enhancing the H_2 yield, which is consistent with the increase in the ratio of H_2 to CO in the high light intensity in Fig. 1d. Under dark conditions, the intensity of the CH_x absorption peak is notably higher than that under light, indicating that after the catalyst completes the process of CH_4, the generated CH_x intermediates produced from CH_4 dehydrogenation are not quickly converted, leading to accumulation on the surface and subsequent reduction in the catalytic rate. The spectra of Ni/KCC-1 catalysts also exhibit a large number of OH and CH_x absorption peaks (Fig. S11, ESI†), further proving that light enhanced the conversion of intermediates and inhibited the side reactions.

3.4. DFT calculations

Using density functional theory (DFT), we established the NiY/KCC-1 model for cross-sectional (Fig. 6a) and side views (Fig. S12, ESI†), respectively. The differential charge distribution *via* DFT calculations, as depicted in Fig. 5b, reveals electron enrichment around Ni and depletion around Y, indicating electron transfer from Y to Ni, consistent with XPS results. Fig. 5c illustrates the density of states (DOS) analysis for the spin-up and spin-down orbitals, showing significant reduction

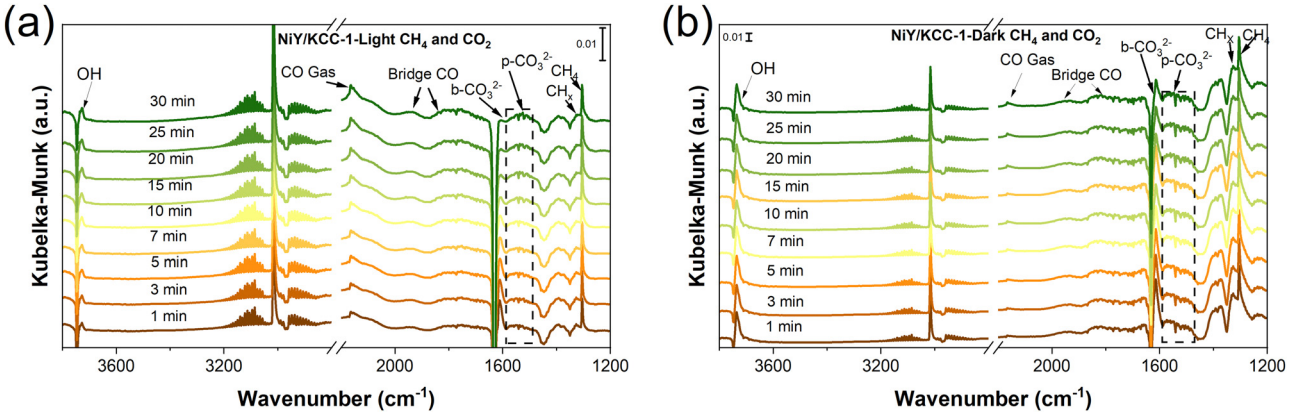

Fig. 5 *In situ* DRIFT spectra of the reaction between CH_4 and CO_2 at various time intervals over NiY/KCC-1 under light (a) and in the dark (b).

in the catalyst's bandgap upon loading Y and Ni, compared to the KCC-1 support. New mixed electronic states emerge near the Fermi level, displaying semi-metallic properties, which can induce surface plasmon resonance and enhance carrier transport, thus improving light utilization. The DOS diagram of NiY/KCC-1 exhibits significant peaks near the Fermi level (−2 to 0 eV) and around 1.5 eV (Fig. 5d), attributed to the hybridization of Ni 3d and O 2p orbitals and electron transfer between Ni 3d and Y 4d orbitals, respectively. This strong d-orbital electron transfer maintains the metallic Ni valence state, ensuring excellent photothermal catalytic DRM performance.

3.5. Reaction mechanism

Based on the characterization and DFT calculations, a reasonable photothermal catalytic DMR mechanism over the NiY/KCC-1 catalyst was proposed. In this catalyst, nickel is present as nanoparticles averaging 4.56 nm, while yttrium is found as partially reduced Y_2O_3. The Y-doped strategy not only facilitates the adsorption and activation of CO_2 but also maintains the metallic Ni valence state through strong d-orbital electron transfer, and therefore more hot electrons are produced *via* the LSPR effect on metallic Ni and then can be injected into the LUMO orbitals of adsorbed CH_4, electronically exciting CH_x species and thereby accelerating the cleavage of the C–H bond.[51] The H* species generated from the dissociation of CH_4 on Ni react with CO_2 to form various intermediates such as CO_3^{2-} and HCOO*. These intermediates further break down to form CO. Under light-assisted conditions, it is favorable for the cleavage of CH_4 to produce H*, but not conducive to the formation of HCOO*, thus avoiding the formation of by-products such as H_2O. It is worth noting that there are many carbonate adsorbates on NiY/KCC-1 under dark conditions, indicating that CO_2 can be adsorbed on YO_x, while Ni sites are active on CH_4. Therefore, the Y-doped NiY/KCC-1 sample can enhance the adsorption and activation of CH_4 and CO_2 by reducing site competition. This bimolecular activation mechanism (L–H mechanism) significantly lowers the reaction energy barrier, thus showing excellent photothermal activity on NiY/KCC-1 (Fig. 7).

4. Conclusion

In summary, the Y-doped nickel-based catalyst NiY/KCC-1 exhibits excellent activity for DRM under photothermal conditions, far surpassing the thermal equilibrium limitation. The photothermal catalytic performance over NiY/KCC-1 can achieve a CO rate of 90 mmol g^{-1} h^{-1} at 450 °C, maintaining stability over 40 hours. Various characterization techniques and DFT theoretical calculations demonstrated that Y-doping enhances CO_2 adsorption and activation, facilitating electron

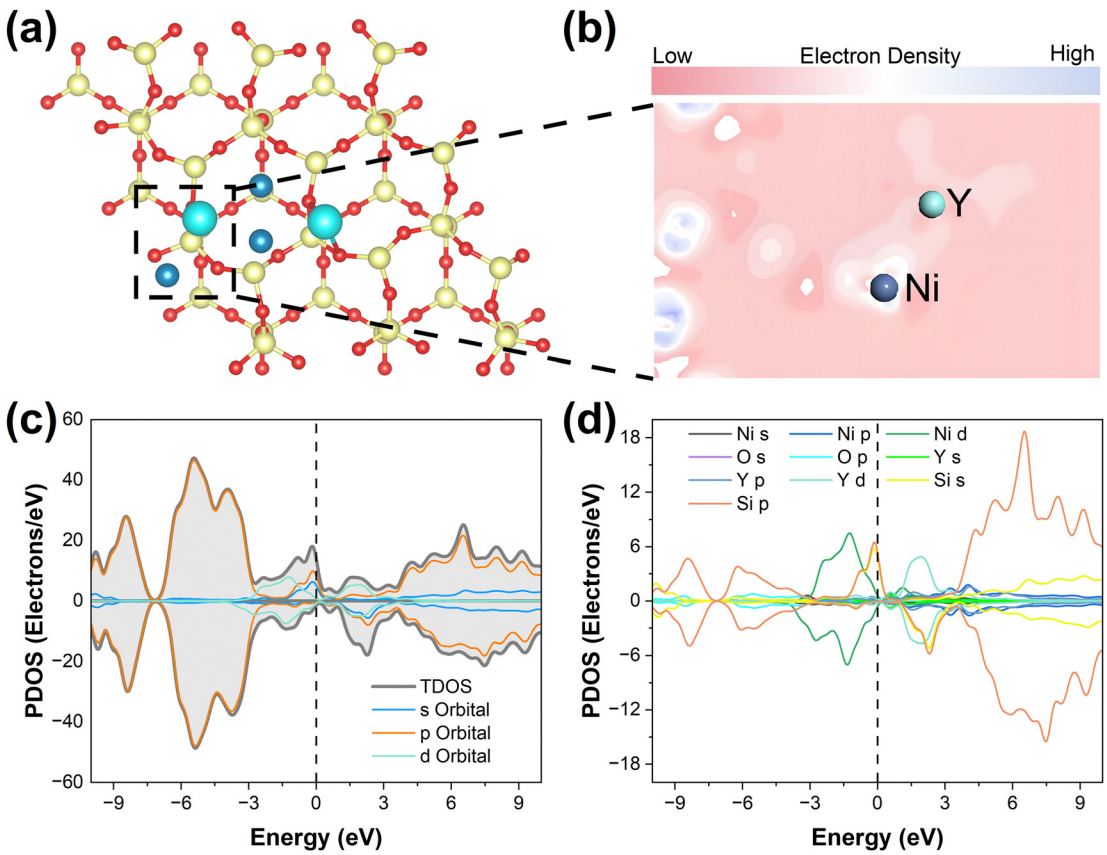

Fig. 6 (a) The NiY/KCC-1 model used for calculation. (b) The differential charge density between the Ni and Y atoms. The (c) total density of states (TDOS) and (d) projected density of states (PDOS) analysis of NiY/KCC-1.

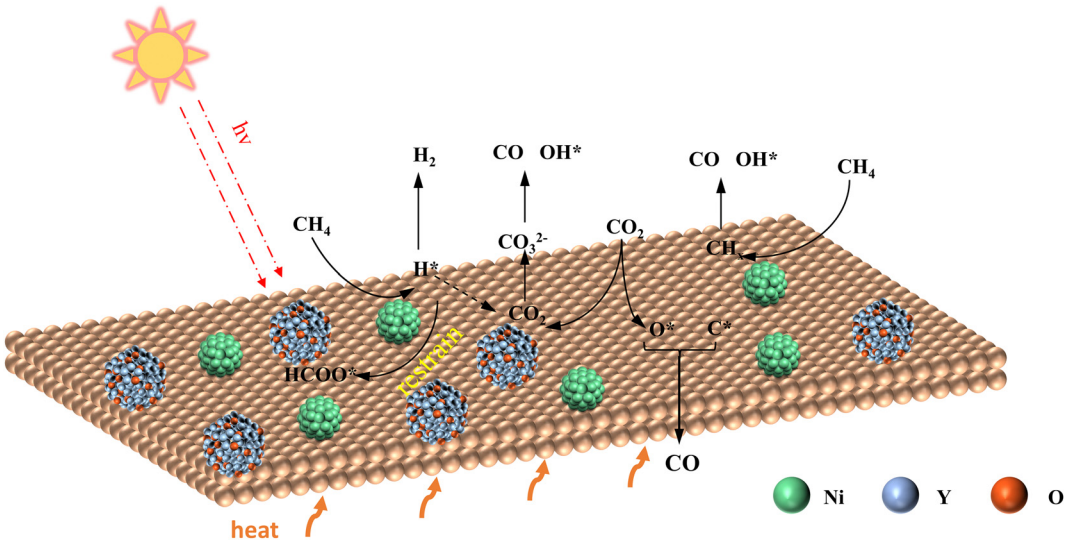

Fig. 7 Tentative mechanism of photothermal MDR on NiY/KCC-1 catalysts.

transfer from Y to Ni in the NiY/KCC-1 catalyst. This d-electron transfer helps Ni retain its metallic state, increases CH_4 active site availability, and significantly boosts the photothermal effect as well, resulting in superior photothermal catalytic performance. Similar rare earth metal doping strategies for the design of efficient photothermal catalysts provide new insights and pave the way for achieving superior catalytic performance by utilizing photothermal synergy.

Author contributions

Xueying Zhang: methodology, verification, formal analysis, investigation, data sorting, and manuscript writing. Zeshu Zhang: resources, ideas, writing, reviews, and editing. Qishun Wang: commentary and editing. Jianheng Xu: software and methodology. Xinyu Han: writing, reviewing, and editing. Jiakun Wang: software. Jia Liu: reviewing and editing. Cheng Rao: editing. Yibo Zhang: conceptualization. Xiangguang Yang: methodology. Lu Wang: methodology, commentary, and editing.

Data availability

The authors declare that the data supporting the findings of this study are available within the paper and its ESI† files. Should any raw data files be needed in another format they are available from the corresponding author upon reasonable request.

Conflicts of interest

The authors declare no conflicts of interest.

Acknowledgements

All authors appreciate the support from the National Natural Science Foundation of China (22208270, 52304429, 22472178, 22072141, 22302206, and 22176185), the National Key Research and Development Program of China (2022YFB3504200), the Jiangxi Provincial Key Research and Development Program (20232BBG70012), the Jiangxi Province "Gan-Po Talent Support Program" (20243BCE51073 and 20243BCE51160), the Natural Science Foundation of Jiangxi Province for Distinguished Young Scholars (20232ACB213004), the Natural Science Foundation of Jiangxi Province (20242BAB21009, 20244BAB28060, and 20232BAB213010), the Youth Innovation Promotion Association of Chinese Academy of Sciences (2018263), the Jiangxi Province "Double Thousand Plan" (jxsq2020101047), the Research Projects of the Ganjiang Innovation Academy, Chinese Academy of Sciences (E355C001) and the Fundamental Research Fund of the Key Laboratory of Rare Earth, Ganjiang Innovation Academy, Chinese Academy of Sciences (E32PF00121).

Notes and references

1 T. T. P. Pham, K. S. Ro, L. Chen, D. Mahajan, T. J. Siang, U. P. M. Ashik, J.-I. Hayashi, D. Pham Minh and D.-V. N. Vo, *Environ. Chem. Lett.*, 2020, **18**, 1987–2019.
2 S. Imada, X. Peng, Z. Cai, A. Najib, M. Miyauchi, H. Abe and T. Fujita, *Materials*, 2020, **13**, 2044.
3 A. Varotto, U. Pasqual Laverdura, M. Feroci and M. L. Grilli, *Materials*, 2024, **17**, 3809.
4 C. Xu, Q. Tang, W. Tu and L. Wang, *Energy Environ. Sci.*, 2024, **17**, 4461–4480.
5 N. A. K. Aramouni, J. G. Touma, B. A. Tarboush, J. Zeaiter and M. N. Ahmad, *Renewable Sustainable Energy Rev.*, 2018, **82**, 2570–2585.
6 D. Pakhare and J. Spivey, *Chem. Soc. Rev.*, 2014, **43**, 7813–7837.
7 Y. Du, C. Li, Y. Dai, H. Yin and M. Zhu, *Nanoscale Horiz.*, 2024, **9**, 1262–1278.
8 Y. J. Song, S. Guo, P. Xia, F. Sun, Z. X. Chen, S. H. Yang, X. Y. Zhang and T. Zhang, *Nanoscale Horiz.*, 2024, **10**, 16–37.

9 Z. Wang, Z. Mei, L. Wang, Q. Wu, C. Xia, S. Li, T. Wang and C. Liu, *J. Mater. Chem. A*, 2024, **12**, 24802–24838.
10 H. Tian, H. Zhu, Y. Xue, M. Wang, K. Xing, Z. Li, X. J. Loh, E. Ye, X. Ding, B. L. Li, X. Yin and D. T. Leong, *Nanoscale Horiz.*, 2024, **9**, 1190–1199.
11 D. Shen, Z. Li, J. Shan, G. Yu, X. Wang, Y. Zhang, C. Liu, S. Lyu, J. Li and L. Li, *Appl. Catal., B*, 2022, **318**, 121809.
12 C. Dang, J. Luo, W. Yang, H. Li and W. Cai, *Ind. Eng. Chem. Res.*, 2021, **60**, 18361–18372.
13 J. Yang, Z. Cao, Y. Wan, S. Guan, B. Jiang, Y. Yamauchi and H. Li, *Adv. Energy Mater.*, 2024, 2404936.
14 Z. Zou, T. Zhang, L. Lv, W. Tang, G. Zhang, R. Kumar Gupta, Y. Wang and S. Tang, *Fuel*, 2023, 343.
15 R. Colombo, G. Moroni, C. Negri, G. Delen, M. Monai, A. Donazzi, B. M. Weckhuysen and M. Maestri, *Angew. Chem., Int. Ed.*, 2024, 63, e202408668.
16 B. Abdullah, N. A. Abd Ghani and D.-V. N. Vo, *J. Cleaner Prod.*, 2017, **162**, 170–185.
17 Q. Cheng, X. Yao, L. Ou, Z. Hu, L. Zheng, G. Li, N. Morlanes, J. L. Cerrillo, P. Castano, X. Li, J. Gascon and Y. Han, *J. Am. Chem. Soc.*, 2023, **145**, 25109–25119.
18 V. Devaraj, I. A. R. Alvarado, J.-M. Lee, J.-W. Oh, U. Gerstmann, W. G. Schmidt and T. Zentgraf, *Nanoscale Horiz.*, 2025, DOI: 10.1039/D4NH00546E.
19 Z. Xie, Q. Liao, M. Liu, Z. Yang and L. Zhang, *Energy Convers. Manage.*, 2017, **153**, 526–537.
20 S. Tang, L. Ji, J. Lin, H. C. Zeng, K. L. Tan and K. Li, *J. Catal.*, 2000, **194**, 424–430.
21 C. Agrafiotis, H. von Storch, M. Roeb and C. Sattler, *Renewable Sustainable Energy Rev.*, 2014, **29**, 656–682.
22 C. He, Q. Li, Z. Ye, L. Wang, Y. Gong, S. Li, J. Wu, Z. Lu, S. Wu and J. Zhang, *Angew. Chem., Int. Ed.*, 2024, 63, e202412308.
23 Z. Chen, M. Pan, C. Cheng, J. Luo and X. Deng, *SusMat*, 2024, **4**, e232.
24 R. Li, T. Takata, B. Zhang, C. Feng, Q. Wu, C. Cui, Z. Zhang, K. Domen and Y. Li, *Angew. Chem., Int. Ed.*, 2023, 62, e202313537.
25 P. Wang, R. Shi, J. Zhao and T. Zhang, *Adv. Sci.*, 2024, **11**, e2305471.
26 H. G. Jin, P. C. Zhao, Y. Qian, J. D. Xiao, Z. S. Chao and H. L. Jiang, *Chem. Soc. Rev.*, 2024, **53**, 9378–9418.
27 Z. Zhu, W. Guo, Y. Zhang, C. Pan, J. Xu, Y. Zhu and Y. Lou, *Carbon Energy*, 2021, **3**, 519–540.
28 Y. Zhang, C.-Q. Cheng, C.-G. Kuai, D. Sokaras, X.-L. Zheng, S. Sainio, F. Lin, C.-K. Dong, D. Nordlund and X.-W. Du, *J. Mater. Chem. A*, 2020, **8**, 17471–17476.
29 X. Chen, Y. Guo, J. Li, H. Yang, Z. Chen, D. Luo and X. Liu, *Chem. Eng. J.*, 2024, **496**, 153947.
30 Z. Li, R. Ma, Q. Ju, Q. Liu, L. Liu, Y. Zhu, M. Yang and J. Wang, *Innovation*, 2022, **3**, DOI: 10.1016/j.xinn.2022.100268.
31 J. Zhang, K. Xie, Y. Jiang, M. Li, X. Tan, Y. Yang, X. Zhao, L. Wang, Y. Wang, X. Wang, Y. Zhu, H. Chen, M. Wu, H. Sun and S. Wang, *ACS Catal.*, 2023, **13**, 10855–10865.
32 M. D. Anker, M. J. Evans, S. A. Cameron and G. Laufersky, *Polyhedron*, 2024, **247**, 116741.
33 A. Maity and V. Polshettiwar, *ChemSusChem*, 2017, **10**, 3866–3913.
34 M. Dhiman and V. Polshettiwar, *J. Mater. Chem. A*, 2016, **4**, 12416–12424.
35 H.-Y. Zheng, Z.-Y. Zhang, K.-D. Xu, S. Wang, B. Yu and T. Xie, *Chem. Eng. J.*, 2022, **428**, 131441.
36 Y. Shi, L. Wang, M. Wu and F. Wang, *Appl. Catal., B*, 2023, **337**, 122927.
37 M. Mao, Q. Zhang, Y. Yang, Y. Li, H. Huang, Z. Jiang, Q. Hu and X. Zhao, *Green Chem.*, 2018, **20**, 2857–2869.
38 Y. Liu, Y. Chen, Z. Gao, X. Zhang, L. Zhang, M. Wang, B. Chen, Y. Diao, Y. Li, D. Xiao, X. Wang, D. Ma and C. Shi, *Appl. Catal., B*, 2022, **307**, 121202.
39 K. Lorber, J. Zavašnik, J. Sancho-Parramon, M. Bubaš, M. Mazaj and P. Djinović, *Appl. Catal., B*, 2022, **301**, 120745.
40 Z. Rao, Y. Cao, Z. Huang, Z. Yin, W. Wan, M. Ma, Y. Wu, J. Wang, G. Yang, Y. Cui, Z. Gong and Y. Zhou, *ACS Catal.*, 2021, **11**, 4730–4738.
41 Y. Wang, L. Yao, Y. Wang, S. Wang, Q. Zhao, D. Mao and C. Hu, *ACS Catal.*, 2018, **8**, 6495–6506.
42 X. Liu, J. Wen, Y. Xie, Z. Li, M. Zhong, R. Nie, S. Peng, J. Cao, J. Chen, P. Ning and Q. Zhang, *Chem. Eng. J.*, 2024, **493**, 152499.
43 J. Zhu, W. Shao, X. Li, X. Jiao, J. Zhu, Y. Sun and Y. Xie, *J. Am. Chem. Soc.*, 2021, **143**, 18233–18241.
44 Z. Pu, Q. Liu, C. Chen and F. Wang, *Chem. Eng. J.*, 2024, **497**, 154861.
45 D. He, J. Yan, K. Chen, L. Zhang, J. Lu, J. Liu and Y. Luo, *ACS Catal.*, 2023, **13**, 12114–12124.
46 H. Wang, G. Cui, H. Lu, Z. Li, L. Wang, H. Meng, J. Li, H. Yan, Y. Yang and M. Wei, *Nat. Commun.*, 2024, **15**, 3765.
47 X. Liu, Q. Gu, Y. Zhang, X. Xu, H. Wang, Z. Sun, L. Cao, Q. Sun, L. Xu, L. Wang, S. Li, S. Wei, B. Yang and J. Lu, *J. Am. Chem. Soc.*, 2023, **145**, 6702–6709.
48 H. Chen, S. Chansai, S. Xu, S. Xu, Y. Mu, C. Hardacre and X. Fan, *Catal. Sci. Technol.*, 2021, **11**, 5260–5272.
49 D. Mao, H. Zhang, J. Zhang and D. Wu, *Chem. Eng. J.*, 2023, **471**, 144605.
50 K. Sun, X. Wu, Z. Zhuang, L. Liu, J. Fang, L. Zeng, J. Ma, S. Liu, J. Li, R. Dai, X. Tan, K. Yu, D. Liu, W. C. Cheong, A. Huang, Y. Liu, Y. Pan, H. Xiao and C. Chen, *Nat. Commun.*, 2022, **13**, 6260.
51 N. Sun, X. Liu, C. Tian, Q. Xu and Y. Xuan, *Adv. Energy Mater.*, 2024, **18**, 8452–8462.